Role of sea surface physical processes in mixed-layer temperature changes during summer marine heat waves in the Chile-Peru Current System

Kylene M. Cooley[1], Melanie R. Fewings[1], James A. Lerczak[1], Larry A. O'Neill[1], Kevin S. Brown[2,3]

[1]College of Earth, Ocean and Atmospheric Sciences, Oregon State University, Corvallis, OR
[2]Department of Chemical, Biological, and Environmental Engineering, Oregon State University, Corvallis, OR
[3]Department of Pharmaceutical Sciences, Oregon State University, Corvallis, OR

Key Points:

- Extreme warm anomalies on time scales greater than 10 days occur mostly in December through March.
- Temperature change from the net surface heat flux anomaly during warm events does not explain most of the anomalous warming.
- Wind stress was weakened over the area of positive anomalous warming, which may contribute to mixed-layer shoaling.

Corresponding author: Kylene M. Cooley, `cooleyky@oregonstate.edu`

Abstract

We identified anomalously high sea surface temperature (SST) events during the 40-year period 1980–2019 near the Punta Lavapié upwelling center in the Chile-Peru Current System (CPCS). Annual distributions of SST anomalies, taken from fifth generation European Centre for Medium-Range Weather Forecasts (ECMWF) reanalysis (ERA5), by season and month indicated that warm SST anomalies were most likely to occur in the austral summer (December through February). At the time of peak warming before the strongest 37 events, we estimated a surface mixed-layer anomaly heat budget with the mean rate of total SST anomaly change and mean rate of SST anomaly change from the net surface heat flux anomaly. The mean net surface heat flux anomaly over the 37 historical warming events was too small to account for most of the maximum rate of anomalous warming. We propose that the weakened surface wind stress observed at the times of maximum warming could amplify the effect of the positive summertime net surface heat flux through mixed-layer shoaling or reduce cold water entering the mixed-layer via entrainment at the base of the surface mixed-layer. This interpretation is based on similarities between the composite mean anomalies of wind stress at the time of peak warming preceding these 37 events in the CPCS and the anomaly fields during previous studies of weak wind events in the California Current System (CCS). Future studies should further investigate the behavior and influence of the surface wind stress and mixed-layer evolution during warm SST anomaly events.

Plain Language Summary

Extreme SST events in and offshore of the Chile-Peru Current System (CPCS) over the last 40 years are characterized in this work by using changes in sea surface temperature relative to the long-term average annual cycle as a measure of heat transfer to the ocean surface mixed layer. We compared events in the CPCS to wind-driven anomalous warming events in the California Current System (CCS) that have similar spatial patterns. Extreme warm events occurred primarily in the austral summer (December through February). The net atmosphere-ocean heat flux does not fully explain the maximum rate of sea surface temperature change in advance of warming events. Reduced mixing at the base of the ocean surface mixed-layer and a shallower mixed-layer depth may be responsible for the observed rapid warming of the upper ocean leading to extreme SST events. We observed reduced wind stress magnitude over the area of maximum warming, and similar ocean surface heat budget studies for the CCS found that reduced mixing and shallower mixed layer depth were likely responsible for warming during weakened winds. This work provides insight into the role of air-sea interactions in driving extreme sea surface temperature anomalies in the CPCS.

1 Introduction

1.1 Marine Heat Waves in the Chile-Peru Current System and California Current System

Marine heat waves (MHWs) are periods of unusually warm sea surface temperatures (SST), or warm anomalies, that occur on a range of time scales of days to months (Hobday et al., 2018). High SST anomaly events such as MHWs are capable of reducing populations of copepods and microphytoplankton, and of threatening dependent fisheries of the southeast Pacific Ocean (Iriarte & González, 2004), similar to the 2014-2016 MHW that altered biological activity in the California Current System (CCS) (Whitney, 2015; McCabe et al., 2016; Cavole et al., 2016; Peterson et al., 2017; Du & Peterson, 2018). MHWs in eastern boundary upwelling systems (EBUS) have the potential to make surface waters too hot for typical local fish populations and the larvae that will become the stock in future years (Cheung & Frölicher, 2020). Those fish that do not perish may migrate to cooler waters far away, as resulted from the 2013-2015 MHW in the CCS (Bond

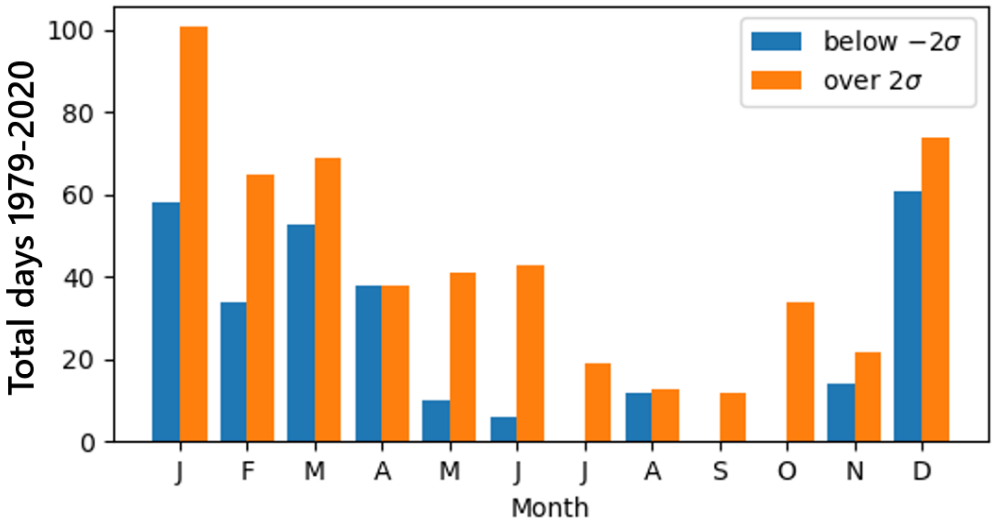

Figure 1. Annual distribution of extreme SST anomalies SST' near 36°S off the coast of Chile. Anomalies are filtered to retain anomalies with time scales greater than seven days. Only SST anomalies that exceeded two standard deviations from zero are included, with positive anomalies in orange and negative anomalies in blue.

et al., 2015; Cavole et al., 2016; Daly et al., 2017; Auth et al., 2018). The Chile-Peru Current System (CPCS) is the most productive EBUS in the world based on fish harvested per unit area (Montecino & Lange, 2009). Due to the biological significance of the Punta Lavapié upwelling center as a food and bait source, we limited this study to only focus on the strongest events affecting this area. An important component in protecting this natural resource is long-term monitoring and comprehension of the processes that drive anomalous environmental variability, such as temperature, that could put strain on the fisheries.

The forcing mechanisms that dominate the surface ocean heat budget during extremely warm SST anomaly events are not clear in the Chile-Peru EBUS. Currently, there is not enough buoy coverage in the CPCS to track increasing surface temperatures as warm anomaly events develop (Garreaud et al., 2011). This study uses reanalysis SST, wind stress magnitude, and other measurements derived from satellite data that are used to estimate how much heat passes through the air-sea interface. The annual distribution of extreme positive SST anomalies off central Chile (Figure 1) indicates that the highest SST anomalies occur most often in December through March, the austral summer, or upwelling season. The tendency of events to occur in summer is reminiscent of anomalous warming events in the CCS that are forced by wind relaxations (Flynn et al., 2017). Propagating atmospheric cyclones weaken upwelling favorable winds in the summer months of May through August in the CCS, leading to the wind relaxations (Halliwell & Allen, 1987; Fewings et al., 2016). A composite surface mixed-layer anomaly heat budget over many wind relaxation events in the CCS was used to highlight the most important processes that contribute to warming SST (Flynn et al., 2017). We are interested in which of the terms in the surface mixed-layer anomaly heat budget equation contribute most to the rate of increasing SST during warm events in the CPCS.

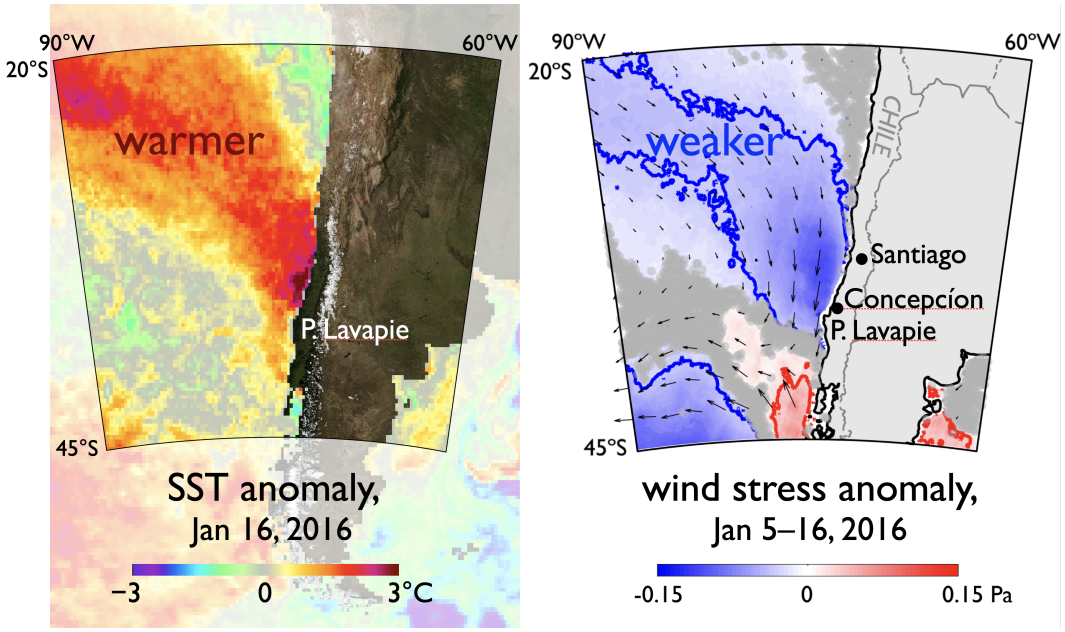

Figure 2. A January 2016 marine heat wave event and preceding wind stress anomaly. (a) Daily SST anomaly off western South America on 16 January 2016, relative to the daily climatology during 2003–2014, from the daily 25-km resolution Multiscale Ultrahigh Resolution (MUR25) L4 product from NASA's State of the Ocean (`http://podaac-tools.jpl.nasa.gov/soto`). (b) Mean wind stress anomaly during 5–16 January 2016, from L2 satellite ocean vector wind stresses from RapidSCAT and ASCAT-A, relative to the climatology for 5–16 January 2000–2017 from QuikSCAT and ASCAT-A, calculated similarly to Fewings and Brown (2019).

1.2 Patterns of a Prolonged Warm Anomaly Event

Remotely sensed unfiltered SST anomalies in the CPCS revealed a significant warm SST anomaly event in January of 2016 (Figure 2). The highest daily SST anomalies (Figure 2a) were at least 3°C, and SST anomalies in this area were paired with weak wind stress anomalies (Figure 2b). Both the positive SST anomaly and negative wind stress anomaly extended spatially offshore to the northwest from the Punta Lavapié upwelling center near the coast.

Wind patterns over the CPCS are similar to winds over the CCS during wind relaxations as atmospheric low pressure systems occur over the ocean. The wind direction is predominantly equatorward (Figure 3) and the strength of alongshore wind stress in this direction primarily determines the strength of coastal upwelling in the CPCS (Bakun & Nelson, 1991). West to east propagating anticyclones form coastal lows at 30°S over the coast of Chile such that the winds relax or reverse to flow offshore around 40°S while the coastal lows evolve (Garreaud et al., 2002). The Chilean Upwelling Experiment (CUpEx) off north-central Chile documented the stable southerly wind climatology and warming of 0.5°C-1°C per day during weak or reversed winds (Garreaud et al., 2011). Our study region includes areas south of the CUpEx study area, which is known to have more frequent weather systems pass along the mid-latitude storm track south of 30°S (Garreaud et al., 2011).

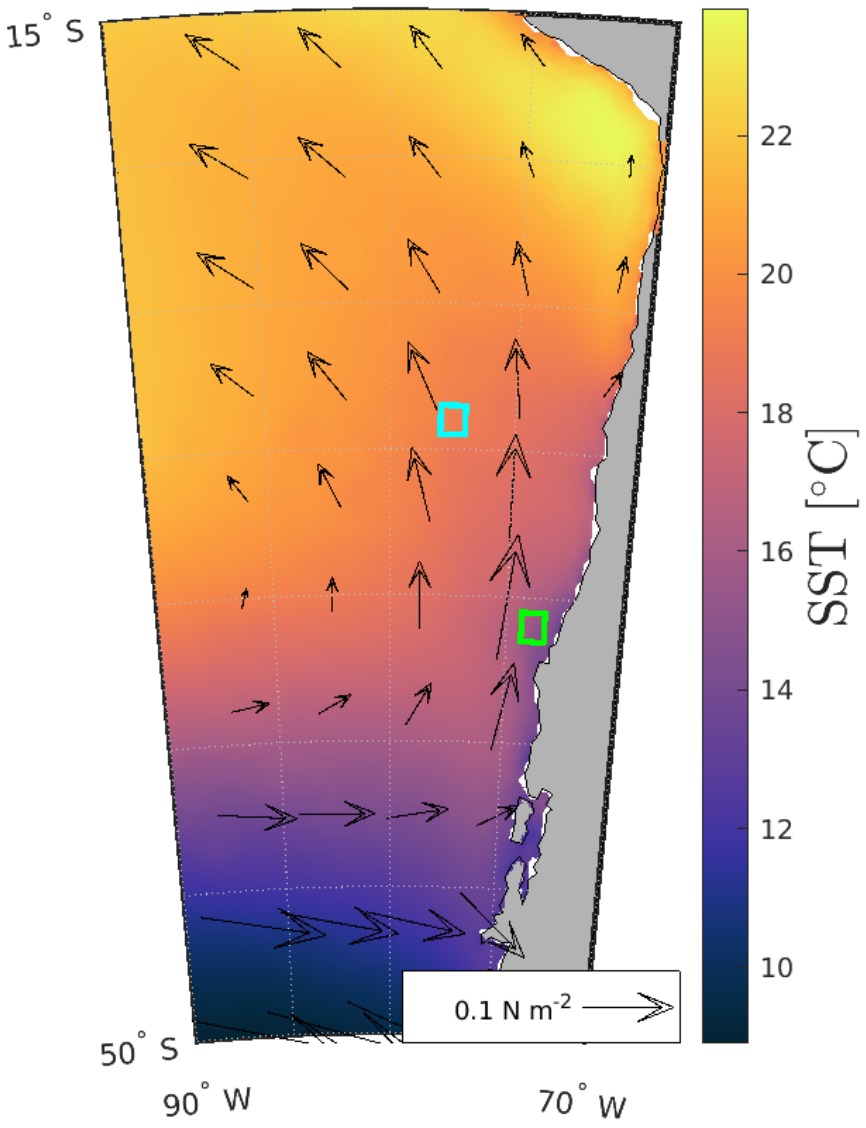

Figure 3. Mean summer SST with arrows illustrating mean summer 10-m wind stress in the Chile-Peru Current System. The green box shows the area where we calculated a mean time series to define SST anomaly events (see section 2.6). The cyan box is the area used for the offshore spatially-averaged time series described in section 2.6.

1.3 Connections to MHW Events in the CCS

In the California Current System (CCS), SST anomalies and surface wind stress anomalies exhibited dipole patterns during wind relaxations. Conditional averages of a surface mixed-layer anomaly heat budget on different days of the wind relaxation event cycle described in Fewings et al. (2016) over many events revealed SST anomalies that divided the CCS into northern and southern regions (Flynn et al., 2017). During wind relaxation events in the poleward (northern) half of the CCS, the net surface heat flux, especially latent heat flux, was the dominant contributor to positive SST anomalies (Flynn et al., 2017). During the wind relaxation phase in the southern (equatorward) region, SST anomalies during wind relaxation events were preconditioned to be colder than average, but still increased from heating during the relaxation south of Cape Mendocino (Flynn et al., 2017, their Figure 8c, day 5), likely via decreased entrainment and Ekman pumping at the base of the mixed layer, and in the California Current extension region, reduced advection of cold water from farther north. Flynn et al. (2017) proposed decreased entrainment and Ekman pumping contributed to warming the most, as the contribution of air-sea heat flux anomalies did not explain the change in SST.

The pattern of strong warm SST anomaly and weak wind stress anomaly connected to an upwelling center in the January 2016 event in the CPCS (Figure 2) was similar to a July 2015 MHW in the CCS. In that event, the wind stress anomaly and SST anomaly extended southwest from Cape Mendocino (Fewings & Brown, 2019), a known upwelling center (Largier et al., 1993). In the case of the July 2015 MHW in the CCS, a longer than average wind relaxation event cycle prolonged the warming conditions so that the spatial pattern of the SST anomaly was similar to the wind stress anomaly (Fewings & Brown, 2019). In contrast, the composite average southern phase of wind relaxation events in the CCS only displayed the same pattern as the wind stress anomaly in the change of the SST anomaly over a five-day event since SST was preconditioned to be cooler in the northern wind relaxation phase (Flynn et al., 2017). Flynn et al. (2017) inferred from the wind field evolution that mixed layer temperature changes were forced by decreased vertical entrainment and mixed layer shoaling since the net surface heat flux was small and advective terms were likely negligible more than several hundred km offshore (Flynn et al., 2017; Correa-Ramirez et al., 2007). If warm SST anomaly events in the CPCS satisfy this condition, other anomalously warm events may be similar to the January 2016 event (Figure 2).

1.4 Research Questions

The goal of this analysis is to provide an explanation for how warm SST anomalies in the CPCS form without the effects of El Niño or long-term SST trends and to compare and contrast CPCS warm events with those in the CCS. This study used a surface mixed-layer anomaly heat budget under the assumption that SST approximated the mixed-layer temperature to answer the research questions:

1. Is the area of anomalous warming for other historical warm SST anomaly events in the CPCS similar in shape and location to the January 2016 warm event (Figure 2)?
2. Does the anomalous warming pattern coincide with a weak wind stress anomaly pattern as in the warm SST anomalies during wind relaxations in the CCS?

2 Data and Methods

2.1 Data

Unfiltered data with 0.25° spatial resolution from 1979-2020 was retrieved from the 5th generation European Centre for Medium-Range Weather Forecasts (ECMWF) Re-

analysis (ERA5) (Hersbach et al., 2018) for the southeast Pacific within 15°S to 50°S and 70°W to 90°W. To resolve sub-monthly time scales, we used time series of daily averages of SST, the daily averages of the northward and eastward components of the accumulated hourly surface wind stress, and the daily averages of the accumulated hourly components of the net surface heat flux (section 2.4). These were obtained from the single level sea surface dataset of ERA5 (Hersbach et al., 2018).

The rate of warming, or partial time derivative of SST, is approximated from SST with the centered difference approximation:

$$\frac{\partial SST}{\partial t}(t_i) \approx \frac{SST(t_i + \Delta t) - SST(t_i - \Delta t)}{2\Delta t}, \tag{1}$$

where Δt is the one-day time interval between data points, and t_i is the time of a discrete observation in the time series.

2.2 Calculating Wind Stress Magnitude

The surface wind stress magnitude was calculated because weakened winds, regardless of wind direction, may contribute to mixed layer shoaling through reduced shear-driven mixing (Price et al., 1986). Previous analyses of anomalously warm events in the CCS have noted that mixed layer shoaling could amplify the warming from the net surface heat flux (Flynn et al., 2017; Fewings & Brown, 2019). The surface wind stress magnitude $|\vec{\tau}|$ was calculated from the ERA5 eastward and northward components of the hourly accumulated wind stress, τ_x and τ_y, by

$$|\vec{\tau}| = \sqrt{\tau_x^2 + \tau_y^2}. \tag{2}$$

Then the daily average of the wind stress magnitude was evaluated afterwards.

2.3 Calculating Daily Anomalies

Daily anomalies were computed by removing long-term daily mean values at each grid point over the 42-year base period between January 1979 through the end of December 2020 by day of year. This process is applied to each location for the time series of SST, $\partial SST/\partial t$, the components of the surface heat flux Q_{net} (section 2.4), and the wind stress magnitude $|\vec{\tau}|$. The daily anomalies computed in this way are denoted by primes hereafter as SST', $\partial SST'/\partial t$, the components of Q'_{net}, and $|\vec{\tau}|'$.

2.4 Estimating Net Surface Heat Flux Anomalies

The net surface heat flux anomaly Q'_{net} is the sum of the anomalies of the four components of the surface heat flux into the ocean. The ERA5 daily anomalies of the turbulent sensible and latent heat fluxes and the net longwave and shortwave radiative fluxes are the four components used to calculate the net surface heat flux anomaly. The net surface heat flux anomaly Q'_{net} is positive when heat is added to the ocean surface mixed-layer through the sea surface by the sum of the anomalous net shortwave radiation into the ocean (Q'_{SWR}), anomalous net longwave radiation (Q'_{LWR}), sensible heat transfer anomalies (Q'_{SHF}), or latent heat anomalies (Q'_{LHF}):

$$Q'_{net} = Q'_{SWR} + Q'_{LWR} + Q'_{SHF} + Q'_{LHF} \ . \tag{3}$$

2.5 Filtering

The daily anomalies were band-pass filtered by applying the low-pass PL66 filter (R. C. Beardsley et al., 1985) twice to isolate signals occurring on time scales between 10 days and 6 months. By restricting this study to events with time scales longer than

10 days, rather than five days as in the Hobday et al. (2016) definition, the anomalously warm events in this study may be better compared with similar extreme events such as the July 2015 event in the CCS, which lasted multiple weeks (Fewings & Brown, 2019). Since our events do not necessarily meet the widely-used Hobday et al. (2016) definition of MHWs, we refer to events as warm SST anomaly events, anomalously warm events, or variations of this henceforth. Removing the seasonal cycle and long-term trends with the high-pass cutoff of 6 months allows us to keep as much variability as possible while maintaining our focus on events that we can compare to wind relaxation events in the CCS.

In the time domain, PL66 is a piecewise parabolic and linear weighting function, giving the transfer function a sharp frequency cutoff and smaller and narrower side lobes than a Lanczos filter (R. C. Beardsley et al., 1985). The first pass used a single PL66 filter as a low-pass filter with half amplitude cutoff frequency at $f_0 = 1.16 \times 10^{-6}$ Hz, or 1 cycle per 10 days. To use PL66 as a high-pass filter, in the second pass the half-amplitude cutoff frequency was $f_0 = 6.34 \times 10^{-8}$ Hz, or 1 cycle per 6 months, and the difference between the once-filtered time series and twice-filtered time series yielded the band-pass filtered signal. After filtering and removing two high-pass window lengths from each end, this data set spans the period of January 1980 through the end of December 2019.

The regional-scale dynamics within a single EBUS in this study are better observed without the overlying influence of the El Niño Southern Oscillation (ENSO) or other warming and wind processes with periods longer than a year. The band-pass filter was applied to SST' to include events obscured by long term trends, on $\partial SST'/\partial t$ and Q'_{net} to observe anomalous warming on these time scales, and on the wind stress magnitude anomaly to show wind stress patterns on the same time scales. The resulting time series for each location did not contain signatures of high-frequency variability such as diurnal warming and short-term wind gusts or variability associated with the seasonal cycle, interannual variability from ENSO, and lower frequencies.

2.6 Defining Warm Events

We define warm SST anomaly events from the highest ∼2.5 percent of SST anomalies in the area offshore of Punta Lavapié. To find events, we used an average of 25 adjacent SST' time series within a 1° by 1° area approximately $50-150$ km offshore as a representative time series (green box in Figure 3). Although this average is taken within the zone that can be influenced by filaments of recently upwelled water, the events found in this time series were very similar in timing to a set of events in the spatial mean of SST' in a box of the same size 200-300 km offshore to the northwest (cyan box in Figure 3). We define warm events as the peaks of positive SST' greater than two standard deviations from the climatological annual cycle (Figure 4). To more easily compare CPCS warm anomaly events with warm events in the CCS that occur in summer, we further focused on just the events occurring in December through February of each year during the austral summer. This restricts our number of independent events to 38 warm events that met this criteria (Cooley, 2021, their Figure 2.2). Although these events are qualitatively similar, we did not use the individual events for additional analyses beyond the conditional average in section 2.8 to illustrate the spatial similarity. A similar spatial average in the same nearshore 1° by 1° area for $\partial SST'/\partial t$ was used to identify the nearest time of peak anomalous warming preceding each maximum in SST' (Figure 4). Due to the first event occurring at the beginning of the band-pass filtered record, there were only 37 times of maximum anomalous warming before warm events (Figure 4). This definition is different from the Hobday definition where MHWs occur when the unfiltered SST is greater than 90% of the values recorded on the same day of year, and the SST remains above this threshold value for at least five consecutive days as the threshold value changes with the climatological SST cycle (Hobday et al., 2016; Oliver et al., 2018).

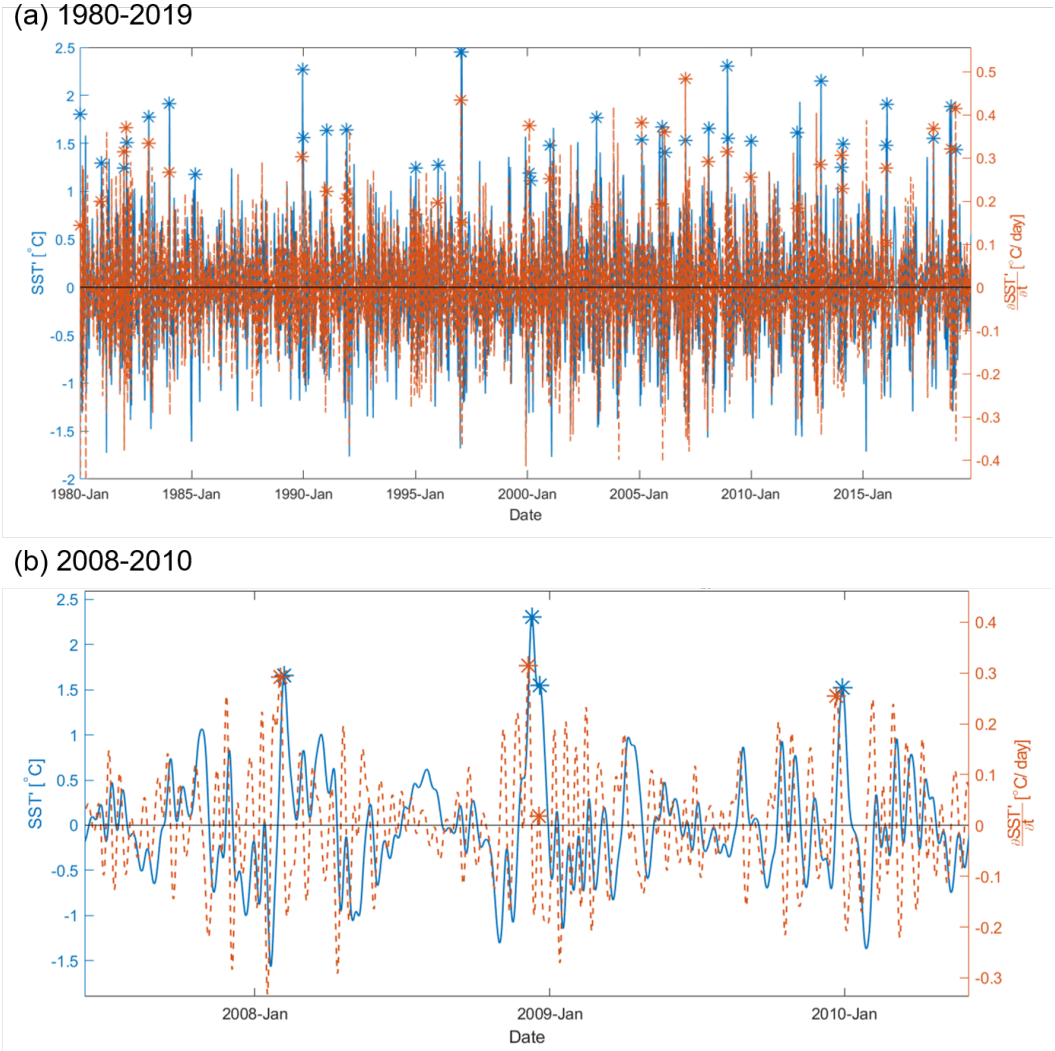

Figure 4. (a) 10-day to six-month band-pass filtered SST anomaly SST' (blue time series) from an average in latitude and longitude over the area where we defined events (green square in Figure 3), and rate of change $\frac{\partial SST'}{\partial t}$ (orange time series) spatially averaged over the same area from ERA5 for warm events detected ∼100 km offshore of the Punta Lavapié upwelling center region. After band-pass filtering (section 2.5), there are 37 events in both time series. (b) A section of the time series from (a) including January 2008 to January 2010.

2.7 Surface Mixed-Layer Anomaly Heat Budget

We used the differential form of the surface mixed-layer anomaly heat budget and absorbed processes not changing temperature through the air-sea interface into a residual term, R, similarly to Flynn et al. (2017); Fewings and Brown (2019):

$$\frac{\partial SST'}{\partial t} = \frac{Q'_{net}}{\rho_w c_p h_0} + R \ . \tag{4}$$

The rate of anomalous SST change $\partial SST'/\partial t$ and the net surface heat flux anomaly Q'_{net} were defined in sections 2.1 and 2.4. The first term on the right side of equation 4 is Q'_{net} divided by the density of seawater, ρ_w, the specific heat capacity of seawater, c_p, and the mixed layer depth (MLD), h_0, which converts Q'_{net} into a rate of temperature change. We used values of $\rho_w = 1025$ kg m^{-3} (Silva et al., 2009; Talley et al., 2011), $c_p = 3850$ J kg^{-1} °C^{-1} (Talley et al., 2011), and $h_0 = 25$ m (Flynn et al., 2017). To isolate the influence of net surface heat flux anomalies, we designated the MLD in equation 4 to be the first term in a Taylor expansion about a constant, climatological MLD, h_0 (section 2.10). Other terms in the expansion which represented corrections to the MLD were incorporated into the residual. Therefore, the residual of the surface mixed-layer heat budget in equation 4 consists of changes to temperature resulting from a combination of penetrating radiation absorbed below the mixed-layer, horizontal advection of temperature, horizontal eddy diffusion of temperature, changes in mixed-layer depth, and entrainment and mixing at the base of the surface mixed-layer, similarly to prior studies (Flynn et al., 2017).

2.8 Compositing Anomalies at Maximum Warming

To understand the cause of high SST' events (blue stars in Figure 4), we examined the surface mixed-layer anomaly heat budget at the time of maximum anomalous warming before those events (orange stars in Figure 4). We found the spatial extent of maximum $\partial SST'/\partial t$ for a typical event by mapping the conditional average of $\partial SST'/\partial t$ at the time of peak warming over the 37 events (orange stars in Figure 4). The values of $\partial SST'/\partial t$ at each of these times of maximum anomalous warming were saved as a daily slice to a data matrix "cube" and then averaged in time. The 95% confidence interval of the mean anomaly at each location is defined by:

$$\mu_y = \hat{\mu}_y \pm \delta\hat{\mu}_y \ , \text{ with } \delta\hat{\mu}_y = \frac{\hat{\sigma}_y}{\sqrt{N}} q_t(\alpha/2, N-1) \tag{5}$$

(Bendat & Piersol, 1986), where μ_y is the true mean, $\hat{\mu}_y$ is the sample mean estimate, and $\delta\hat{\mu}_y$ is the uncertainty in the sample estimate. In the uncertainty, the sample estimate of the standard deviation is $\hat{\sigma}_y$, $\alpha = 0.05$ is the level of significance, $q_t(\alpha/2, N-1)$ is the upper tail of a Student-t distribution at the $\alpha/2$ point with $N-1$ degrees of freedom, and N is the number of degrees of freedom which is equal to 37 for the number of independent events. When mapping the composite anomalies, we applied a mask where this interval included zero to exclude any anomaly that was approximately equal to zero, similarly to Flynn et al. (2017).

A similar conditional average and confidence interval was evaluated for the other anomalies calculated in section 2.3. The anomalous warming from the Q'_{net} term in the anomaly heat budget (equation 4) was averaged at the time of peak anomalous warming $\partial SST'/\partial t$ before each of the 37 events (Figure 4). The difference between the conditional average of $\partial SST'/\partial t$ and the conditional average of the $Q'_{net}/\rho_w c_p h_0$ term yielded the estimate of the mean residual over the 37 events as in equation 4. The difference between the quantities $\partial SST'/\partial t$ and $Q'_{net}/\rho_w c_p h_0$ for individual events was used to find a standard deviation and 95% confidence interval for the residual temperature change, similarly to equation 5. Then, to estimate the mean surface wind stress magnitude anomaly at times of maximum anomalous warming, the same process was used to calculate the

conditional average and confidence interval of the surface wind stress magnitude anomalies (section 2.2). The composite average of SST' at the time of the event provided a mean maximum SST' for anomalously warm events.

2.9 Mixed-Layer Depth Climatology

Our estimate of the contribution of the Q'_{net} term to the rate of anomalous warming depended on the MLD. Our estimate of $h_0 = 25$ m was similar to the MLD used in previous studies (Flynn et al., 2017; Fewings & Brown, 2019) for mid-latitude offshore waters. The offshore regional anomalous warming from the Q'_{net} term was approximated with this MLD since our study area was located in the CPCS around 35°S.

Seasonal MLD values were estimated from Argo float profiles and the Holte et al. (2017) MLD monthly climatological values as a comparison to the approximate value used here. The monthly climatologies contained missing values at locations with not enough Argo profiles sampled. We evaluated the mean of the monthly MLD climatologies for the months of December, January, and February in our study region to find the mean summer climatological MLD. In this step, locations where the MLD for one or more months was missing were also left missing in the summer mean MLD. This ensured that for a summer mean MLD, we would not consider any mean values where an insufficient number of profiles were sampled for at least one of the months such that the other months would bias the summer mean.

2.10 Linear Regression for MLD Assuming No Residual

A linear regression model for the surface mixed-layer anomaly heat budget tested the possibility that the net surface heat flux anomaly term could explain all anomalous warming in equation 4. We considered a case of the surface mixed-layer anomaly heat budget where there is no residual change in SST'. We first calculated the correlation coefficients between $\partial SST'/\partial t$ and $Q'_{net}/\rho_w c_p$ for the 37 events at each location. Then we used the linear regression

$$\frac{Q'_{net}}{\rho_w c_p} = \hat{h}\,\frac{\partial SST'}{\partial t} + \epsilon, \tag{6}$$

where $Q'_{net}/\rho_w c_p$ is modeled as a function of $\partial SST'/\partial t$, $\hat{h}$ is the coefficient of the linear term which defines the best fit line, and ϵ is the error in the model. This linear coefficient $\hat{h}$ is the MLD that would be most consistent with the case where Q'_{net} is responsible for all mixed-layer warming during the warm events. For each location, we calculated the linear coefficient $\hat{h}$ from this regression using the 37 events.

At each location, we also tested whether the skill of the model $\hat{S}$ was greater than the critical skill $\hat{S}_{\mathsf{crit}}$ for a Gaussian distribution for $N = 37$ degrees of freedom. The equations for these are:

$$\hat{S} = \frac{\hat{\sigma}^2_{\hat{y}}}{\hat{\sigma}^2_{y}} \tag{7}$$

and

$$\hat{S}_{\mathsf{crit}}(\alpha, 1, N) = \frac{q_F(\alpha, 1, N-2)}{(N-2) + q_F(\alpha, 1, N-2)} \tag{8}$$

where $\hat{S}$ is the skill of the model at a location, $\hat{\sigma}_{\hat{y}}$ is the sample variance of the linear regression model, and $\hat{\sigma}_y$ is the sample variance of the observations (Emery & Thomson, 2001). For the null hypothesis test, $\hat{S}_{crit}$ is the critical skill level, $\alpha = 0.05$ is the significance level, $N = 37$ is the number of degrees of freedom, and $q_F(\alpha, 1, N-2)$ is the upper tail of the Fisher-F distribution for a univariate linear regression (Emery & Thomson, 2001). At any location where $\hat{S} < \hat{S}_{crit}$, a MLD estimate $\hat{h}$ for the linear regression model was not determined.

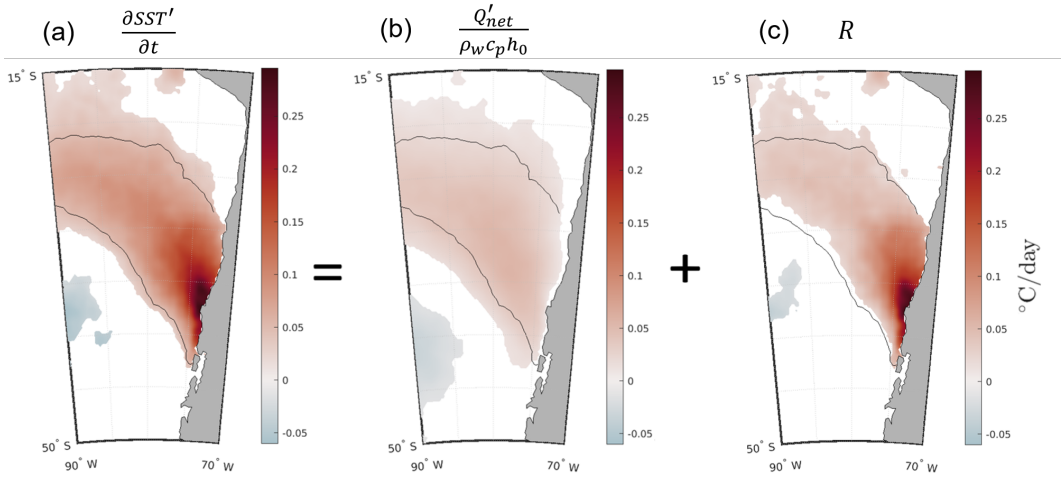

Figure 5. The heat budget (equation 4) where the sum of the composite mean anomalous warming over 37 events from $Q'_{net}/\rho c_p h_0$ (b) and the residual temperature change R (c) equals the composite mean $\partial SST'/\partial t$ over 37 events (a). White indicates composite anomalies that do not differ from zero by more than half the width of the 95% confidence interval on the mean. The black contour line indicates $\partial SST'/\partial t = 0.05$°C day^{-1}.

3 Results

3.1 Spatial Pattern of Anomalous Warming Events

Based on the spatial similarities between the wind stress anomaly and SST anomaly in the January 2016 CPCS event (Figure 2), we hypothesized that the spatial pattern of maximum $\partial SST'/\partial t$ for the composite average warm event in the CPCS around 40°S would be a band reaching offshore towards the northwest from the Punta Lavapié upwelling center as in the January 2016 warm event SST anomaly. On average, the maximum anomalous warming preceding warm events offshore of the Punta Lavapié upwelling center (Figure 5a) occurred in a geographically similar area to the positive SST anomaly pattern during the January 2016 warm event in the GHRSST satellite imagery (Figure 2a). The area affected by anomalously strong warming was a concave south band $\sim$ 280 km wide reaching offshore to the northwest. There was a small ($\sim$ 110 km across) patch of anomalous cooling to the south of the band of warming, about 300 km offshore. The strongest anomalous warming was concentrated in an area northwest of Punta Lavapié within 75 km of the coast, while most of the anomalous warming offshore was contained in a band 200-250 km wide, which is outlined by the black line in Figure 5a that denotes 0.05 °C day^{-1} in anomalous warming. Rates of anomalous warming in the area closest to the coast were greater than 0.25 °C day^{-1}, and in the offshore anomalous warming reached rates between 0.05-0.15 °C day^{-1}.

The composite average of SST' over the 37 events illustrates that the highest anomalies over 1.6 °C tend to be localized near the coast north of Punta Lavapié (Figure 6). In contrast, the highest offshore anomaly along, for example, 80°W between 15°S and 50°S is 0.7 °C, less than half as warm, though it is still significantly different from zero. The small area of negative $\partial SST'/\partial t$ on the southwest side of Figure 5a implies that a not insignificant rate of anomalous cooling is common in that area during warming events off Punta Lavapié, although this was not enough cooling to materialize negative SST' (no blue area in Figure 6).

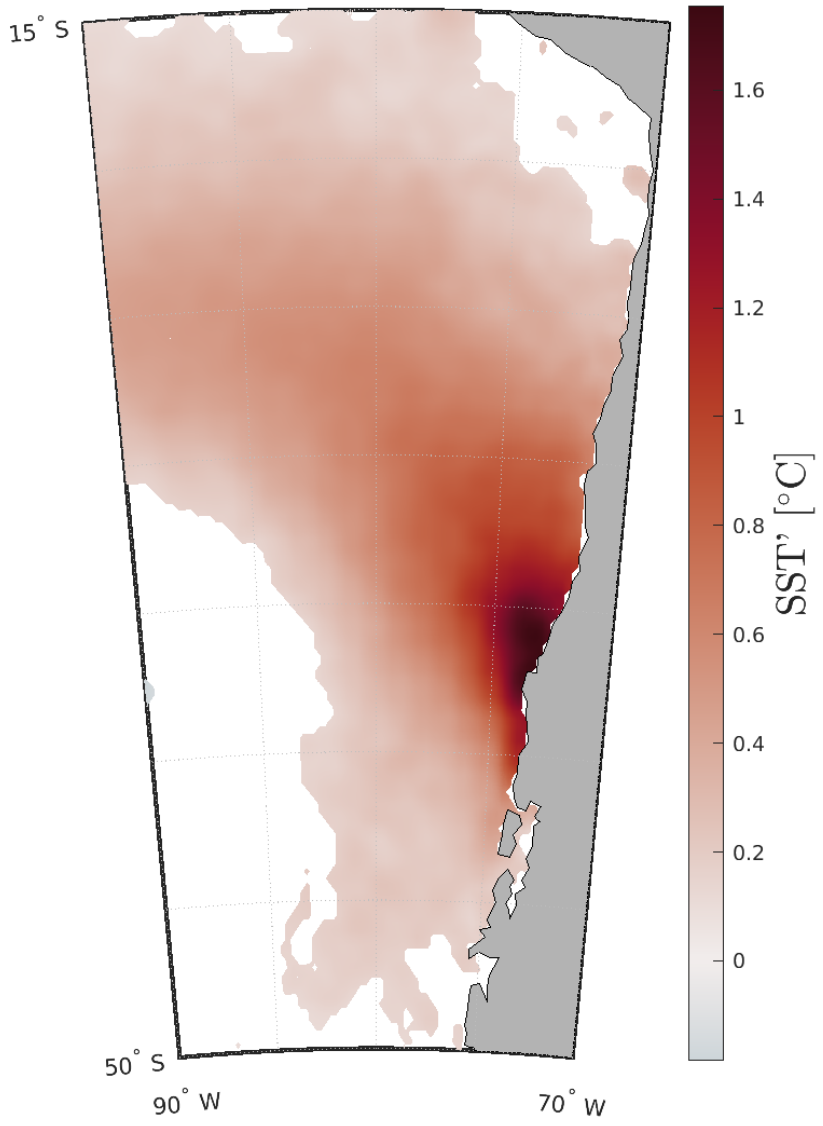

Figure 6. Composite average of SST' over 37 events (blue stars in Figure 4). White indicates anomalies not exceeding the uncertainty in the mean. SST' was band-pass filtered to retain temporal variability with time scales between 10 days and six months.

3.2 Mean Rates of Warming From the Anomaly Heat Budget Terms

The anomalous rate of temperature change from the net surface heat flux anomaly term preceding warm events was small compared to the total rate of anomalous warming. From the 37 events, the mean rate of anomalous warming from the net surface heat flux anomaly term (Figure 5b) was generally below 0.05 °C day^{-1}, which is small compared to the observed warming in the previous section. The gap between positive values and the coast indicates that the net surface heat flux anomaly term Q'_{net} does not contribute significantly to temperature change near the coast. The area of significant mean anomalous warming from the Q'_{net} term has a similar pattern to the positive $\partial SST'/\partial t$ region: warming from the net surface heat flux anomaly term is in the center of the black outline of anomalous warming, extending from the upwelling center towards the northwest (Figure 5b). Anomalous warming from the Q'_{net} term affects a larger area than $\partial SST'/\partial t$ preceding SST' events (Figure 5b). Within several 100 km of the coast, the residual in the anomaly heat budget, R, is much greater than the temperature change from Q'_{net} (Figure 5c). Farther offshore, the residual is still substantial, approximately the same value as $Q'_{net}/\rho_w c_p h_0$.

3.3 Effect of Mixed-Layer Depth on Warming

The impact of the net surface heat flux anomaly term in our 1-D surface mixed-layer anomaly heat budget depends on the mixed-layer depth (MLD) since we assume the density and the specific heat capacity are constant. A shallower MLD could allow the net surface heat flux to be solely responsible for anomalously large SST' increases as the residual in the heat budget trends towards zero. Under the assumption that $R = 0$ (as in equation 4), the linear regression of the total anomalous rate of change in SST' onto the anomalous warming from the net surface heat flux anomaly yielded the best-fit MLD. The linear regression model was a good fit in most of the study area, as the correlation coefficients between $Q'_{net}/\rho_w c_p$ and $\partial SST'/\partial t$ were greater than the critical value for statistical significance at the 95% confidence level, $\hat{\rho}_{crit} = 0.325$ (Figure 7). Only in regions nearest to the coast, where the skill of the model was less than the critical skill $\hat{S}_{crit} = 0.11$ (Figure 8), were $Q'_{net}/\rho_w c_p$ and $\partial SST'/\partial t$ not significantly correlated with 95% confidence. The section of the coast north of Punta Lavapié where the residual was large in Figure 5c was one such area, so a MLD in the $R = 0$ case was not determined.

Using the linear regression model from section 2.10, the coefficient of the linear term $\hat{h}$, or slope of the line, was mapped over the study region as a best-fit estimate of the MLD under the assumption that there is no residual rate of anomalous temperature change (Figure 8). In most of the offshore area where there is a positive rate of anomalous warming preceding events, we found that the mixed layer depth would need to be between 2 and 7 meters if the net surface heat flux anomaly produced all of the temperature change (Figure 8). The best-fit mixed layer depth from the linear regression model only reaches a maximum slightly above 11 meters in the area where the net surface heat flux anomaly is near zero (Figure 5b). In contrast, Figure 9 illustrates how most of the typical MLD values for the austral summer fall around 30 meters within the red $\partial SST'/\partial t = 0.05$ °C day^{-1} line. An average of all summer mixed-layer depths in the study domain weighted by the area of each square yielded an average mixed layer depth of about 23 m. Since the MLD from the Holte et al. (2017) climatology is much greater than the linear regression MLD, it is not possible for the net surface heat flux anomaly term to explain most of the anomalous warming during our events unless the MLD during these events is only ∼1/3 as deep as typical summer MLDs.

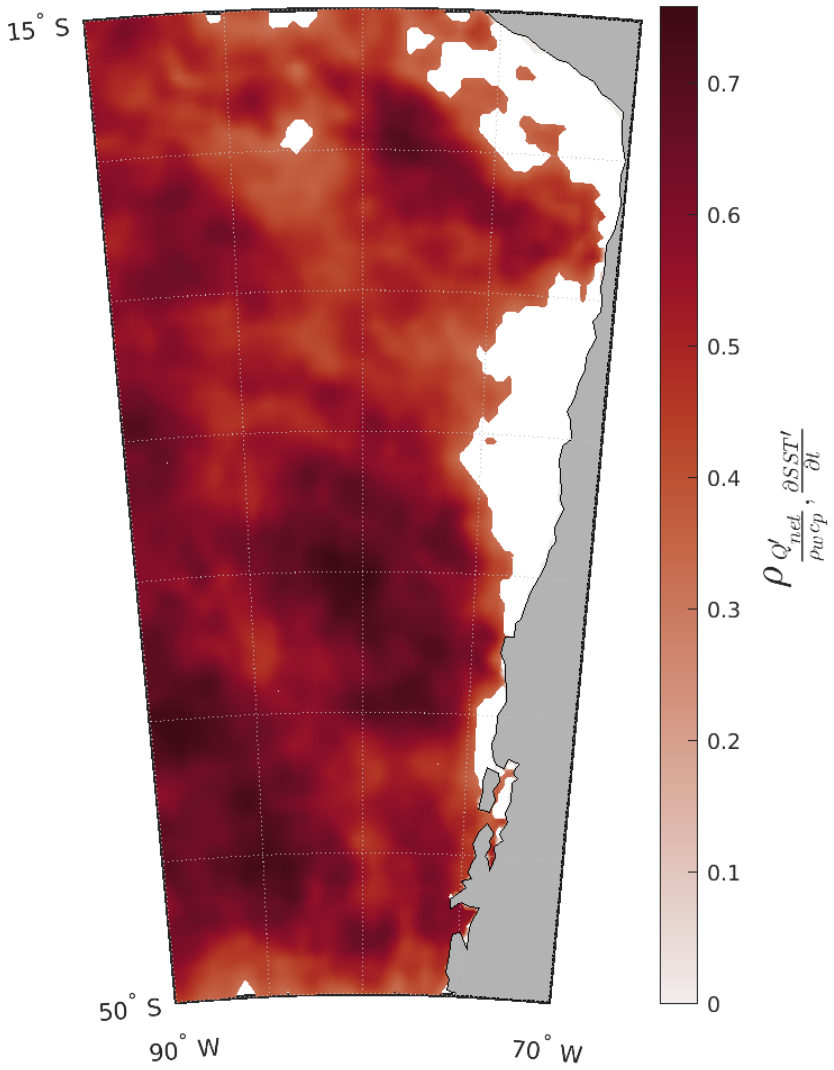

Figure 7. Correlation coefficients between the net surface heat flux anomaly Q'_{net} and rate of change of SST anomaly $\partial SST'/\partial t$ at the times of peak anomalous warming during the 37 events. Correlation coefficients that are not above the critical value $\hat{\rho}_{crit} = 0.325$ are shown in white.

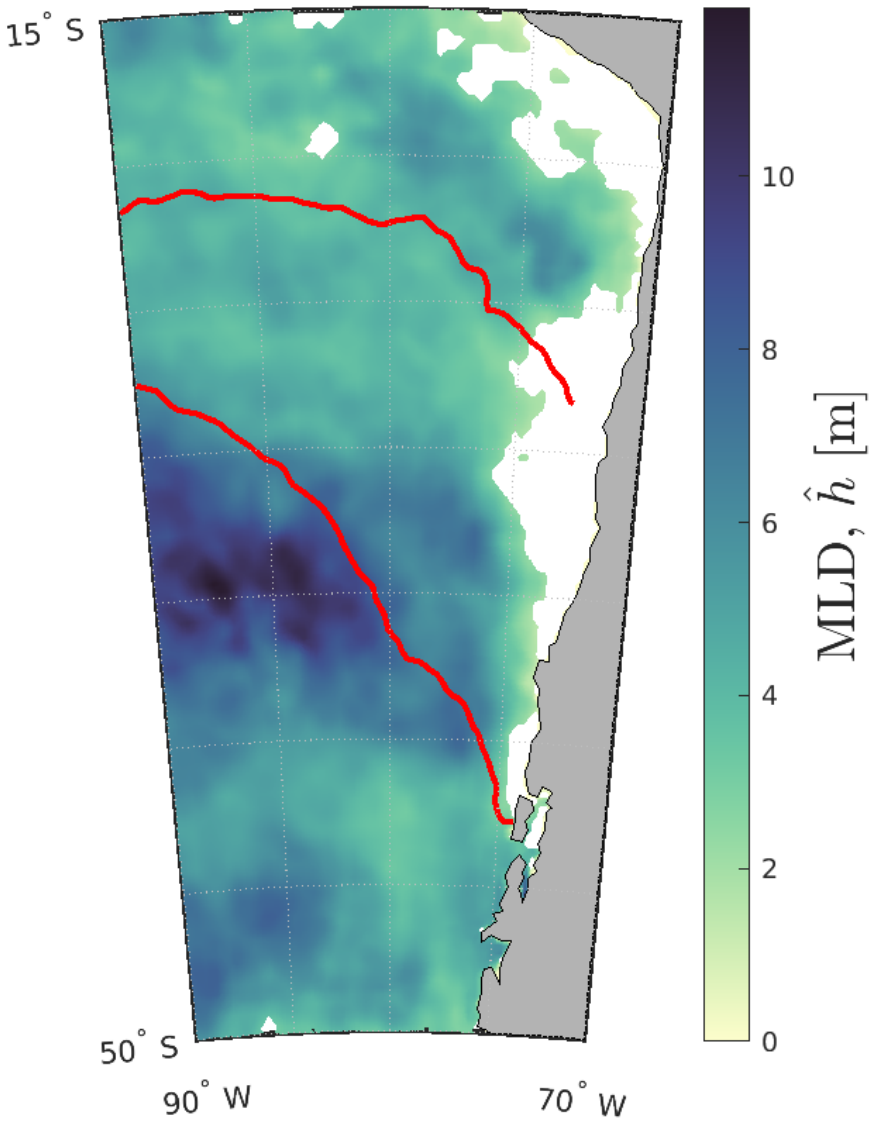

Figure 8. A map of the best-fit mixed layer depth (MLD) $\hat{h}$ from equation 6, which is the MLD that would be necessary in the heat budget (equation 4) in the case that all anomalous temperature change was due to the net surface heat flux anomaly absorbed in the mixed-layer. The white areas are where the skill of the linear regression is less than the critical skill $\hat{S}_{crit} = 0.11$.

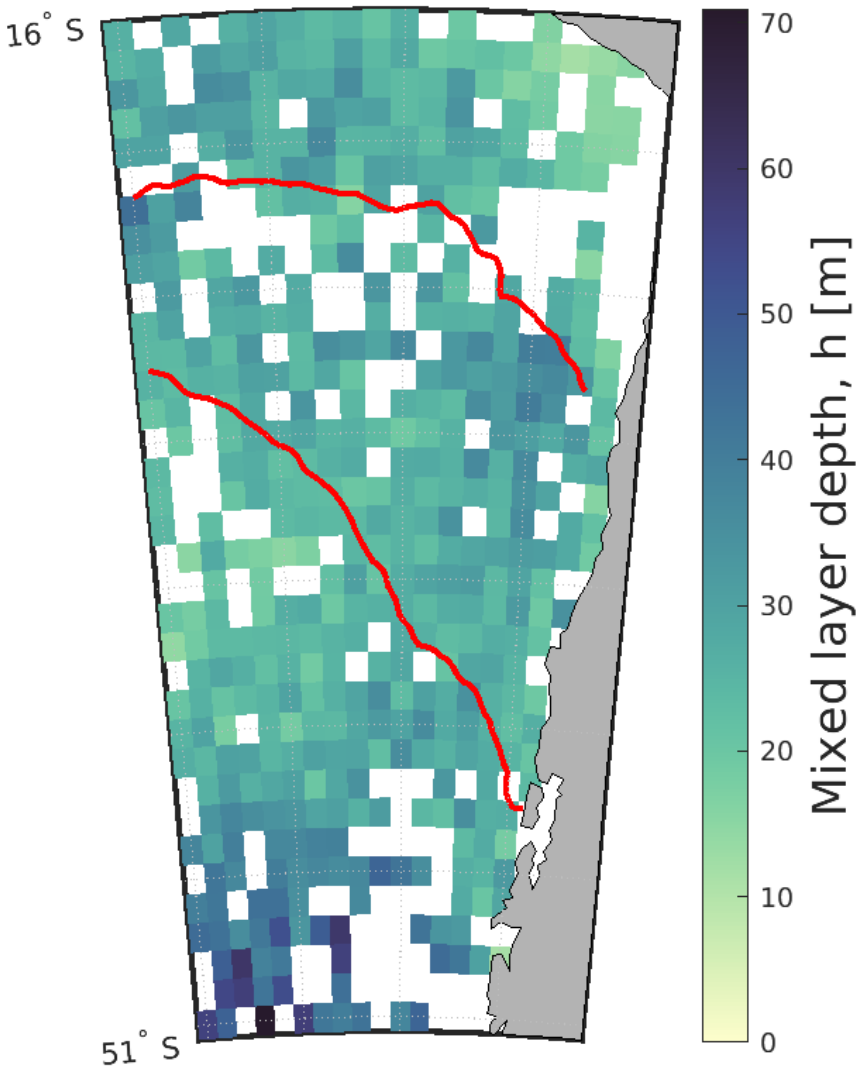

Figure 9. Seasonal climatology of MLD in summer, the mean MLD at each grid location over December, January, and February from the monthly MLD climatology from Holte et al. (2017). The blank squares are where there were not enough Argo profiles taken in any one month to find a valid MLD climatological value. The red line shows the outline of the region where $\partial SST'/\partial t = 0.05°\text{C day}^{-1}$. This color bar scale has a range approximately seven times bigger than than the range of the color bar in Figure 8.

3.4 Wind Stress Anomaly Patterns Preceding Warm Events

The surface wind stress magnitude anomaly was used to map the mean surface wind stress magnitude anomaly (Figure 10) over the 37 times of peak anomalous warming (orange stars in Figure 4). In the area where $\partial SST'/\partial t$ is positive (within the red outline in Figure 10), the wind stress magnitude anomaly is negative, indicating weakened wind stress. A smaller positive wind stress magnitude anomaly area to the south is separated from the northern negative wind stress magnitude anomaly by an area where there is no significant wind stress magnitude anomaly about 40 km wide across the whole study region. There is also a small negative anomaly area in the southwest corner of the study region (Figure 10).

4 Discussion

4.1 Anomalous Warming Residual and MLD

The anomalous warming from the net surface heat flux anomaly term with a constant MLD had a statistically significant mean spatial structure similar to $\partial SST'/\partial t$. This motivated us to determine whether the net surface heat flux anomaly is the dominant term balancing $\partial SST'/\partial t$ in the anomalous heat budget. As shown in section 3.2, the anomalous temperature change from the mean net surface heat flux anomaly term during historical warm events (Figure 5b) was small compared to what would be needed to explain the observed anomalous warming (Figure 5a). This result was dependent on the MLD in the mid-latitude CPCS which we initially assumed was $h_0 = 25$ m. The red outline in Figure 9 surrounds most of the area of anomalous warming over all 37 events. In this area the mean summer MLDs are all deeper than our linear regression estimate of MLDs from equation 6. At all locations where $\hat{h}$ is significant, the mixed layer depth would need to be at most 11 m, or half as deep as the average mixed layer-depth in summer in the mid-latitudes (Figure 8). It does not appear to be reasonable that anomalous sea surface temperature change in advance of warm events can be explained entirely by the net surface heat flux anomaly unless the mixed layer depth is much shallower than typical for these locations and season. Assuming that changes in the mixed layer depth are dependent on changes in wind-driven mixing, without preexisting shallow MLDs a change in the predominant surface wind stress in advance of the peak rate of warming for each event is necessary to attain the observed anomalous rate of warming if the net surface heat flux anomaly is small.

4.2 Offshore Warming From Other Processes

As mentioned in section 2.7, the residual, or amount of anomalous warming not explained by the net surface heat flux anomaly, includes $\partial SST'/\partial t$ from penetrating shortwave radiation anomalies that are absorbed below the mixed layer, horizontal advection of SST' gradients, horizontal eddy diffusion, temporal and advective changes in MLD, and entrainment and mixing with colder water at depth $z = -h$. Anomalies of penetrating radiation are likely negligible as argued in Flynn et al. (2017) for the CCS because the shortwave radiative flux anomaly at the surface is small within the net surface heat flux anomaly and SWR at depth $z = -h$ is a fraction of this. Outside of the upwelling zone, farther than approximately 200-300 km offshore (Bakun & Nelson, 1991; Montecino & Lange, 2009), we do not expect advection by the mean flow or by eddies to play a large role in the heat budget (Subramanian et al., 2013), so a major contribution from advection of MLD or SST' gradients is unlikely. This leaves the vertical terms in the residual, decreased entrainment and mixed layer shoaling, which were inferred to be a substantial contribution to part of the heat budget in the CCS in Flynn et al. (2017).

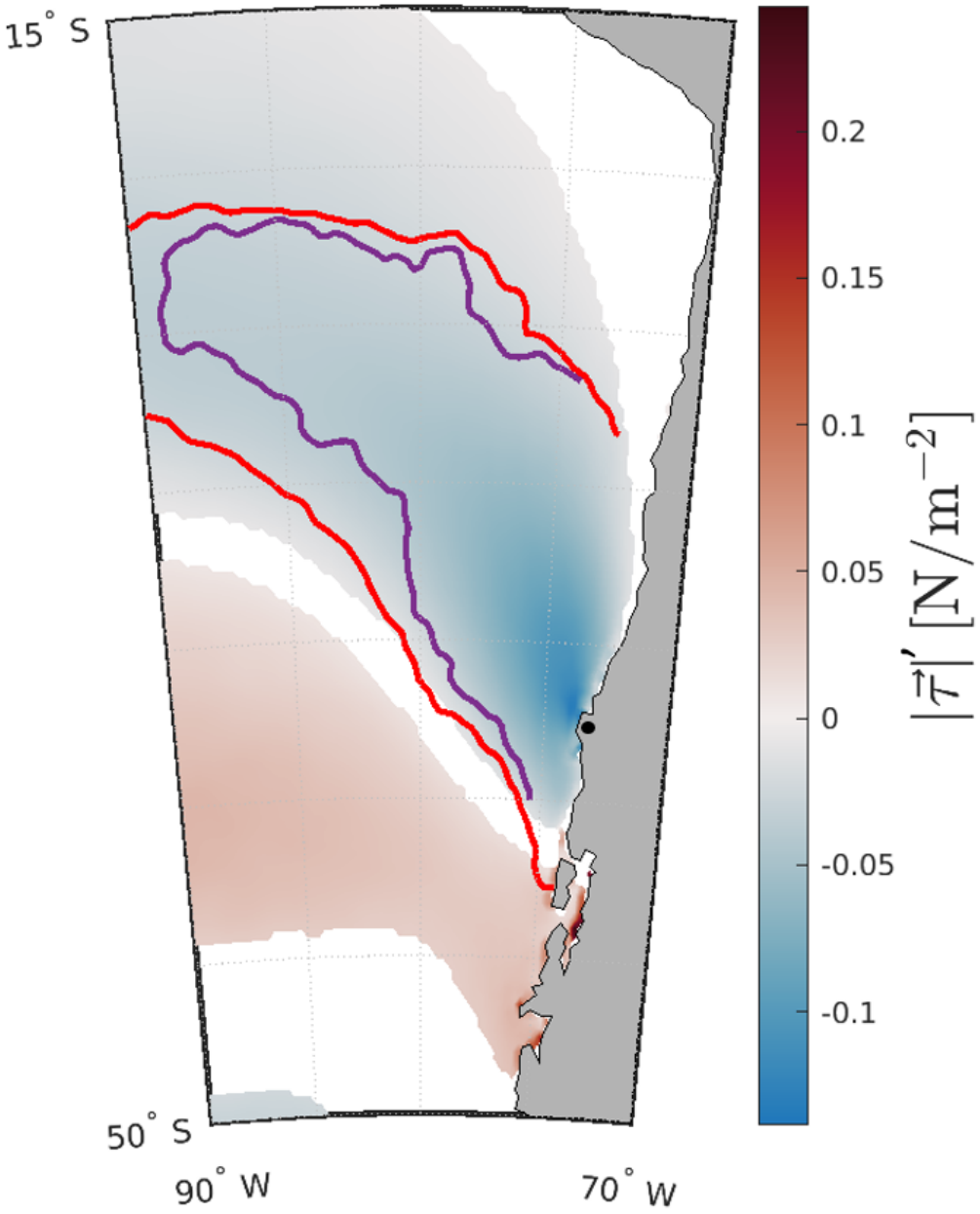

Figure 10. Average 10-day to 6-month band-pass filtered wind stress magnitude anomaly over 37 events at the time of peak anomalous warming. Anomalies not significantly different from zero with 95% confidence are shown in white. The red line is the $\partial SST'/\partial t = 0.05$ °C day^{-1} contour, and the purple line is the $R = 0.04$ °C day^{-1} contour.

4.3 Negative Wind Stress Anomalies Co-Located With Anomalous Warming

The mean wind stress magnitude anomaly is negative at the time of the mean peak anomalous warming in the contour that encloses most of the anomalous warming (red line in Figure 10) and in the contour around most of the residual (purple line in Figure 10). There is a significant negative wind stress magnitude anomaly north of Punta Lavapié, nearer to the coast, which is over some of the area where a MLD estimate could not be determined with the assumption $R = 0$ because the linear regression model did not have statistically significant skill. Since in this area near the coast north of Punta Lavapié changing the MLD could not explain the residual using the net surface heat flux anomaly term (i.e., they are not linearly related), there is likely some other process contributing to the warm anomalies here that does not scale with the net surface heat flux anomaly, most likely reduced coastal upwelling.

For the offshore areas in the anomalous warming region, mixed layer shoaling likely contributes to enhanced warming based on the reduced wind stress magnitude (Price et al., 1986) and the arguments in section 4.2. In section 4.1 we concluded that the observed climatological summer (DJF) MLDs were not consistent with the net surface heat flux anomalies explaining all of $\partial SST'/\partial t$. The negative surface wind stress magnitude anomaly during times of warming (Figure 10) could however lead to shoaling in MLD so that the climatological and anomalous net surface heat fluxes would heat an anomalously shallow mixed layer, resulting in anomalous warming and helping to explain the residual in the heat budget. Additionally, abnormally low surface wind stress magnitude may decrease rates of mixing and entrainment at the lower boundary of the mixed-layer to increase rates of warming. The section of positive wind stress magnitude anomaly over the area of anomalous cooling in the southwest (Figure 10) is potentially an example of the opposite case in action. The surface wind stress anomaly-SST' relationship illustrated by Figure 10 is good motivation for future studies to quantify the contributions of wind stress in the mid-latitude CPCS surface mixed-layer anomaly heat budget during anomalously warm events.

5 Conclusion

If future events are likely to shift towards current extremes (Intergovernmental Panel on Climate Change, 2012), focusing on the highest 2.5% of SST anomalies provides a good long-term estimate of future major warm events in the CPCS, as was proposed for extreme MHWs in the CCS (Fewings & Brown, 2019). The composite of the surface mixed-layer anomaly heat budget during warm events off Punta Lavapié improved understanding of the spatial structure of warm events in the CPCS by revealing the large offshore extent of the area of significant anomalous warming. Areas where the composite anomalous warming was significantly positive may be increasingly prone to high SST anomalies as strong warm events occur more frequently.

The net surface heat flux anomaly term of the heat budget could not explain all anomalous warming in the CPCS, and order of magnitude estimates similar to Flynn et al. (2017) indicated the likelihood that reduced entrainment at the base of the mixed-layer and MLD shoaling could contribute the most to anomalous warming offshore. Reduced wind stress contributes to both reduced entrainment and MLD shoaling (Price et al., 1986). Negative wind stress magnitude anomalies in the high anomalous warming area motivate future investigation of wind stress on time scales of 10 days to six months for the CPCS. Most events on time scales of 10 days to six months that affected our study area were detected in the austral summer, which is similar in timing to wind relaxations in the CCS, which are more likely to occur in the boreal summer (Fewings et al., 2016). This comparison of the surface mixed-layer anomaly heat budgets of two EBUS in the

Pacific Ocean illustrates how the application of similar methods might be used to compare anomalously warm events globally.

Open Research

The ERA5 single-level data used for anomalies of SST, the net surface heat flux, and the wind stress magnitude in the study are available at the ECMWF Copernicus Climate Change Service (C3S) Climate Data Store (CDS) via `https://doi.org/10.24381/cds.adbb2d47` with the License to Use Copernicus Products and a free account (Hersbach et al., 2018). The temperature algorithm monthly mean mixed-layer depth data used for the map of summer mean mixed-layer depth in the study are freely available at `mixedlayer.ucsd.edu` from the University of California San Diego (Holte et al., 2017, last accessed: 15 June 2021). Design of the PL66 low-pass filter weights is described in R. C. Beardsley et al. (1985), and the code for the PL66 filter is available on GitHub under the MIT License at `https://github.com/sea-mat/bobstuff/blob/master/pl66tn.m` (B. Beardsley, 2000). PODAAC L4 MUR data for SST anomalies in Figure 2 is openly shared by PO.DAAC via `https://doi.org/10.5067/GHGMR-4FJ04` (Chin et al., 2017; JPL MUR MEaSUREs Project, 2019). The ASCAT and RapidScat scatterometer winds in Figure 2 are also available from PO.DAAC via `https://podaac.jpl.nasa.gov/dataset/ASCATA-L2-Coastal` and `https://doi.org/10.5067/RSX12-L2C11` (Verhoef & Stoffelen, 2013; EUMETSAT/OSI SAF, 2010; RapidScat Project, 2016).

Acknowledgments

This research was funded by NASA Ocean Vector Winds Science Team grant number 80NSSC18K1611 to Melanie Fewings. We thank Emily Hayden, Andrew Mandovi, and Yi-Wei (Michael) Chen for feedback on the manuscript. Perceptually-uniform colormaps from the cmocean package developed by Thyng et al. (2016) were used to make maps visually accessible and to maintain efficacy of our maps in grayscale.

References

Auth, T. D., Daly, E. A., Brodeur, R. D., & Fisher, J. L. (2018). Phenological and distributional shifts in ichthyoplankton associated with recent warming in the northeast Pacific Ocean. *Global Change Biology*, *24*(1), 259–272. Retrieved 2021-12-10, from `https://onlinelibrary.wiley.com/doi/abs/10.1111/gcb.13872` (_eprint: https://onlinelibrary.wiley.com/doi/pdf/10.1111/gcb.13872) doi: 10.1111/gcb.13872

Bakun, A., & Nelson, C. S. (1991, December). The Seasonal Cycle of Wind-Stress Curl in Subtropical Eastern Boundary Current Regions. *Journal of Physical Oceanography*, *21*(12), 1815–1834. Retrieved 2021-06-01, from `https://journals.ametsoc.org/view/journals/phoc/21/12/1520-0485_1991_021_1815_tscows_2_0_co_2.xml` (Publisher: American Meteorological Society Section: Journal of Physical Oceanography) doi: 10.1175/1520-0485(1991)021⟨1815:TSCOWS⟩2.0.CO;2

Beardsley, B. (2000, October). *PL66TN [Software].* GitHub. Retrieved 2021-06-29, from `https://github.com/sea-mat/bobstuff/blob/master/pl66tn.m`

Beardsley, R. C., Limeburner, R., & Rosenfeld, L. K. (1985). Introduction to the CODE-2 moored array and large-scale data report. *CODE-2: moored array and large-scale data report*, 85–35. (Publisher: Woods Hole Oceanographic Institution Technical Report, WHOI-85-35)

Bendat, J. S., & Piersol, A. G. (1986). *Random data: analysis and measurement procedures* (2nd ed.). Wiley-Interscience.

Bond, N. A., Cronin, M. F., Freeland, H., & Mantua, N. (2015). Causes and impacts of the 2014 warm anomaly in the NE Pacific. *Geophysical Re-*

search Letters, *42*(9), 3414–3420. Retrieved 2021-12-10, from https://onlinelibrary.wiley.com/doi/abs/10.1002/2015GL063306 (_eprint: https://onlinelibrary.wiley.com/doi/pdf/10.1002/2015GL063306) doi: 10.1002/2015GL063306

Cavole, L., Demko, A., Diner, R., Giddings, A., Koester, I., Pagniello, C., ... Franks, P. (2016). Biological Impacts of the 2013–2015 Warm-Water Anomaly in the Northeast Pacific: Winners, Losers, and the Future. *Oceanography*, *29*(2). Retrieved 2021-06-15, from https://tos.org/oceanography/article/biological-impacts-of-the-20132015-warm-water-anomaly-in-the-northeast-paci doi: 10.5670/oceanog.2016.32

Cheung, W. W. L., & Frölicher, T. L. (2020, April). Marine heatwaves exacerbate climate change impacts for fisheries in the northeast Pacific. *Scientific Reports*, *10*(1), 6678. Retrieved 2021-06-15, from https://www.nature.com/articles/s41598-020-63650-z (Number: 1 Publisher: Nature Publishing Group) doi: 10.1038/s41598-020-63650-z

Chin, T. M., Vazquez-Cuervo, J., & Armstrong, E. M. (2017, October). A multi-scale high-resolution analysis of global sea surface temperature. *Remote Sensing of Environment*, *200*, 154–169. Retrieved 2021-12-08, from https://linkinghub.elsevier.com/retrieve/pii/S0034425717303462 doi: 10.1016/j.rse.2017.07.029

Cooley, K. M. (2021). *Role of Sea Surface Physical Processes in Mixed-layer Temperature Changes During Summer Marine Heat Waves in the Chile-Peru Current System* (Master's thesis, Oregon State University, Corvallis, OR). Retrieved 2021-12-01, from https://ir.library.oregonstate.edu/concern/graduate_thesis_or_dissertations/xg94hx65c

Correa-Ramirez, M. A., Hormazábal, S., & Yuras, G. (2007). Mesoscale eddies and high chlorophyll concentrations off central Chile (29°–39°S). *Geophysical Research Letters*, *34*(12). Retrieved 2021-11-12, from https://onlinelibrary.wiley.com/doi/abs/10.1029/2007GL029541 (_eprint: https://onlinelibrary.wiley.com/doi/pdf/10.1029/2007GL029541) doi: 10.1029/2007GL029541

Daly, E. A., Brodeur, R. D., & Auth, T. D. (2017, February). Anomalous ocean conditions in 2015: impacts on spring Chinook salmon and their prey field. *Marine Ecology Progress Series*, *566*, 169–182. Retrieved 2021-12-10, from https://www.int-res.com/abstracts/meps/v566/p169-182/ doi: 10.3354/meps12021

Du, X., & Peterson, W. T. (2018). Phytoplankton Community Structure in 2011–2013 Compared to the Extratropical Warming Event of 2014–2015. *Geophysical Research Letters*, *45*(3), 1534–1540. Retrieved 2021-12-10, from https://onlinelibrary.wiley.com/doi/abs/10.1002/2017GL076199 (_eprint: https://onlinelibrary.wiley.com/doi/pdf/10.1002/2017GL076199) doi: 10.1002/2017GL076199

Emery, W. J., & Thomson, R. E. (2001). *Data analysis methods in physical oceanography* (2nd and rev. ed. ed.). Amsterdam ; New York: Elsevier.

EUMETSAT/OSI SAF. (2010). *MetOp-A ASCAT Level 2 Ocean Surface Wind Vectors Optimized for Coastal Ocean Ver. Operational/Near-Real-Time.* PO.DAAC, CA, USA. Retrieved from https://podaac.jpl.nasa.gov/dataset/ASCATA-L2-Coastal

Fewings, M. R., & Brown, K. S. (2019, October). Regional Structure in the Marine Heat Wave of Summer 2015 Off the Western United States. *Frontiers in Marine Science*, *6*, 564. Retrieved 2021-03-08, from https://www.frontiersin.org/article/10.3389/fmars.2019.00564/full doi: 10.3389/fmars.2019.00564

Fewings, M. R., Washburn, L., Dorman, C. E., Gotschalk, C., & Lombardo, K. (2016). Synoptic forcing of wind relaxations at Pt.

Conception, California. *Journal of Geophysical Research: Oceans*, *121*(8), 5711–5730. Retrieved 2021-06-18, from https://agupubs.onlinelibrary.wiley.com/doi/abs/10.1002/2016JC011699 (_eprint: https://agupubs.onlinelibrary.wiley.com/doi/pdf/10.1002/2016JC011699) doi: 10.1002/2016JC011699

Flynn, K. R., Fewings, M. R., Gotschalk, C., & Lombardo, K. (2017, March). Large-scale anomalies in sea-surface temperature and air-sea fluxes during wind relaxation events off the United States West Coast in summer. *Journal of Geophysical Research: Oceans*, *122*(3), 2574–2594. Retrieved 2021-03-08, from http://doi.wiley.com/10.1002/2016JC012613 doi: 10.1002/2016JC012613

Garreaud, R. D., Rutllant, J. A., & Fuenzalida, H. (2002, January). Coastal lows along the subtropical West Coast of South America: Mean structure and evolution. *Monthly Weather Review*, *130*(1), 75. Retrieved 2021-08-21, from http://www.proquest.com/docview/198185855/citation/ACAD8F2A010A4723PQ/1 (Num Pages: 14 Place: Washington, United States Publisher: American Meteorological Society)

Garreaud, R. D., Rutllant, J. A., Muñoz, R. C., Rahn, D. A., Ramos, M., & Figueroa, D. (2011). VOCALS-CUpEx: the Chilean Upwelling Experiment. *Atmospheric Chemistry and Physics*, *11*(5), 2015. Retrieved 2021-08-21, from http://www.proquest.com/docview/857526251/abstract/D030E1C93E4F4E6DPQ/1 (Num Pages: 2015 Place: Katlenburg-Lindau, Germany Publisher: Copernicus GmbH)

Halliwell, G. R., & Allen, J. S. (1987, February). The large-scale coastal wind field along the west coast of North America, 1981–1982. *Journal of Geophysical Research: Oceans*, *92*(C2), 1861–1884. Retrieved 2021-09-08, from https://agupubs.onlinelibrary.wiley.com/doi/10.1029/JC092iC02p01861 (Publisher: John Wiley & Sons, Ltd) doi: 10.1029/JC092iC02p01861

Hersbach, H., Bell, B., Berrisford, P., Biavati, G., Horányi, A., Muñoz Sabater, J., ... Thépaut, J.-N. (2018). *ERA5 hourly data on single levels from 1979 to present.* Copernicus Climate Change Service (C3S) Climate Data Store (CDS). doi: 10.24381/cds.adbb2d47

Hobday, A. J., Alexander, L. V., Perkins, S. E., Smale, D. A., Straub, S. C., Oliver, E. C. J., ... Wernberg, T. (2016, February). A hierarchical approach to defining marine heatwaves. *Progress in Oceanography*, *141*, 227–238. Retrieved 2021-06-18, from https://www.sciencedirect.com/science/article/pii/S0079661116000057 doi: 10.1016/j.pocean.2015.12.014

Hobday, A. J., Oliver, E. C. J., Gupta, A. S., Benthuysen, J. A., Burrows, M. T., Donat, M. G., ... Smale, D. A. (2018). Categorizing and Naming Marine Heatwaves. *Oceanography*, *31*(2), 162–173. Retrieved 2021-06-18, from https://www.jstor.org/stable/26542662 (Publisher: Oceanography Society)

Holte, J., Talley, L. D., Gilson, J., & Roemmich, D. (2017, June). An Argo mixed layer climatology and database. *Geophysical Research Letters*, *44*(11), 5618–5626. Retrieved 2021-07-06, from https://onlinelibrary.wiley.com/doi/10.1002/2017GL073426 doi: 10.1002/2017GL073426

Intergovernmental Panel on Climate Change. (2012). *Managing the Risks of Extreme Events and Disasters to Advance Climate Change Adaptation: Special Report of the Intergovernmental Panel on Climate Change.* Cambridge University Press. (Google-Books-ID: nQg3SJtkOGwC)

Iriarte, J. L., & González, H. E. (2004, March). Phytoplankton size structure during and after the 1997/98 El Niño in a coastal upwelling area of the northern Humboldt Current System. *Marine Ecology Progress Series*, *269*, 83–90. Retrieved 2021-10-27, from https://www.int-res.com/abstracts/meps/v269/p83-90/ doi: 10.3354/meps269083

JPL MUR MEaSUREs Project. (2019). *GHRSST Level 4 MUR 0.25 deg Global Foundation Sea Surface Temperature Analysis. Ver. 4.2.* PO.DAAC, CA, USA. Retrieved 2021-12-07, from https://doi.org/10.5067/GHM25-4FJ42

Largier, J. L., Magnell, B. A., & Winant, C. D. (1993). Subtidal circulation over the northern California shelf. *Journal of Geophysical Research: Oceans*, *98*(C10), 18147–18179. Retrieved 2021-09-15, from http://onlinelibrary.wiley.com/doi/abs/10.1029/93JC01074 (_eprint: https://onlinelibrary.wiley.com/doi/pdf/10.1029/93JC01074) doi: 10.1029/93JC01074

McCabe, R. M., Hickey, B. M., Kudela, R. M., Lefebvre, K. A., Adams, N. G., Bill, B. D., ... Trainer, V. L. (2016). An unprecedented coastwide toxic algal bloom linked to anomalous ocean conditions. *Geophysical Research Letters*, *43*(19), 10,366–10,376. Retrieved 2021-12-10, from https://onlinelibrary.wiley.com/doi/abs/10.1002/2016GL070023 (_eprint: https://onlinelibrary.wiley.com/doi/pdf/10.1002/2016GL070023) doi: 10.1002/2016GL070023

Montecino, V., & Lange, C. B. (2009, December). The Humboldt Current System: Ecosystem components and processes, fisheries, and sediment studies. *Progress in Oceanography*, *83*(1), 65–79. Retrieved 2021-06-17, from https://www.sciencedirect.com/science/article/pii/S0079661109001049 doi: 10.1016/j.pocean.2009.07.041

Oliver, E. C. J., Donat, M. G., Burrows, M. T., Moore, P. J., Smale, D. A., Alexander, L. V., ... Wernberg, T. (2018, April). Longer and more frequent marine heatwaves over the past century. *Nature Communications*, *9*(1), 1324. Retrieved 2021-06-18, from https://www.nature.com/articles/s41467-018-03732-9. doi: 10.1038/s41467-018-03732-9

Peterson, W. T., Fisher, J. L., Strub, P. T., Du, X., Risien, C., Peterson, J., & Shaw, C. T. (2017). The pelagic ecosystem in the Northern California Current off Oregon during the 2014–2016 warm anomalies within the context of the past 20 years. *Journal of Geophysical Research: Oceans*, *122*(9), 7267–7290. Retrieved 2021-12-09, from https://onlinelibrary.wiley.com/doi/abs/10.1002/2017JC012952 (_eprint: https://onlinelibrary.wiley.com/doi/pdf/10.1002/2017JC012952) doi: 10.1002/2017JC012952

Price, J. F., Weller, R. A., & Pinkel, R. (1986). Diurnal cycling: Observations and models of the upper ocean response to diurnal heating, cooling, and wind mixing. *Journal of Geophysical Research: Oceans*, *91*(C7), 8411–8427. Retrieved 2021-09-09, from https://agupubs.onlinelibrary.wiley.com/doi/abs/10.1029/JC091iC07p08411 (_eprint: https://agupubs.onlinelibrary.wiley.com/doi/pdf/10.1029/JC091iC07p08411) doi: 10.1029/JC091iC07p08411

RapidScat Project. (2016). *Rapidscat Level 2B Climate Ocean Wind Vectors in 12.5km Footprints. Ver. 1.0.* PO.DAAC, CA, USA. Retrieved from https://doi.org/10.5067/RSX12-L2C11 doi: 10.5067/RSX12-L2C11

Silva, N., Rojas, N., & Fedele, A. (2009, July). Water masses in the Humboldt Current System: Properties, distribution, and the nitrate deficit as a chemical water mass tracer for Equatorial Subsurface Water off Chile. *Deep Sea Research Part II: Topical Studies in Oceanography*, *56*(16), 1004–1020. Retrieved 2021-07-06, from https://www.sciencedirect.com/science/article/pii/S0967064508004220 doi: 10.1016/j.dsr2.2008.12.013

Subramanian, A. C., Miller, A. J., Cornuelle, B. D., Di Lorenzo, E., Weller, R. A., & Straneo, F. (2013, March). A data assimilative perspective of oceanic mesoscale eddy evolution during VOCALS-REx. *Atmospheric Chemistry and Physics*, *13*(6), 3329–3344. Retrieved 2021-11-13, from https://acp.copernicus.org/articles/13/3329/2013/ doi:

10.5194/acp-13-3329-2013

Talley, L. D., Pickard, G. L., Emery, W. J., & Swift, J. H. O. (2011). *Descriptive physical oceanography: an introduction* (6th ed. ed.). Amsterdam ; Boston: Academic Press.

Thyng, K., Greene, C., Hetland, R., Zimmerle, H., & DiMarco, S. (2016, September). True Colors of Oceanography: Guidelines for Effective and Accurate Colormap Selection. *Oceanography*, *29*(3), 9–13. Retrieved 2021-06-29, from `https://tos.org/oceanography/article/true-colors-of-oceanography-guidelines-for-effective-and-accurate-colormap` doi: 10.5670/oceanog.2016.66

Verhoef, A., & Stoffelen, A. (2013). *Validation of ASCAT coastal winds, version 1.5* (Tech. Rep. No. SAF/OSI/CDOP/KNMI/TEC/RP/176). EUMETSAT. Retrieved 2021-12-10, from `https://knmi-scatterometer-website-prd.s3-eu-west-1.amazonaws.com/publications/ascat_coastal_validation_1.5.pdf`

Whitney, F. A. (2015). Anomalous winter winds decrease 2014 transition zone productivity in the NE Pacific. *Geophysical Research Letters*, *42*(2), 428–431. Retrieved 2021-12-10, from `https://onlinelibrary.wiley.com/doi/abs/10.1002/2014GL062634` (_eprint: https://onlinelibrary.wiley.com/doi/pdf/10.1002/2014GL062634) doi: 10.1002/2014GL062634